PHYSICAL REVIEW B **106**, 165113 (2022)

Enhanced superconductivity and electron correlations in intercalated $ZrTe_3$

Yu Liu (刘育),[1,*] Xiao Tong (佟晓),[2] V. N. Ivanovski,[3] Zhixiang Hu (胡之翔),[1,4] Denis Leshchev,[5]
Xiangde Zhu (朱相德),[1,†] Hechang Lei (雷和畅),[1,‡] Eli Stavitski,[5] Klaus Attenkofer,[5,§] V. Koteski,[3] and C. Petrovic[1,4,‖]
[1]Condensed Matter Physics and Materials Science Department, Brookhaven National Laboratory, Upton, New York 11973, USA
[2]Center of Functional Nanomaterials, Brookhaven National Laboratory, Upton, New York 11973, USA
[3]Department of Nuclear and Plasma Physics, Vinca Institute of Nuclear Sciences - National Institute of the Republic of Serbia, University of Belgrade, Belgrade 11001, Serbia
[4]Materials Science and Chemical Engineering Department, Stony Brook University, Stony Brook, New York 11790, USA
[5]National Synchrotron Light Source II, Brookhaven National Laboratory, Upton, New York 11973, USA

(Received 25 January 2022; revised 25 August 2022; accepted 28 September 2022; published 13 October 2022)

Charge density waves (CDWs) with superconductivity, competing Fermi surface instabilities, and collective orders have captured much interest in two-dimensional van der Waals (vdW) materials. Understanding the CDW suppression mechanism, its connection to the emerging superconducting state, and electronic correlations provides opportunities for engineering the electronic properties of vdW heterostructures and thin-film devices. Using a combination of the thermal transport, x-ray photoemission spectroscopy, Raman measurements, and first-principles calculations, we observe an increase in electronic correlations of the conducting states as the CDW is suppressed in $ZrTe_3$ with 5% Cu and Ni intercalation in the vdW gap. As superconductivity emerges, intercalation brings not only decoupling of quasi-one-dimensional conduction electrons with phonons as a consequence of intercalation-induced lattice expansion but also a drastic increase in Zr^{2+} at the expense of Zr^{4+} metal atoms. These observations not only demonstrate the potential of atomic intercalates in the vdW gap for ground-state tuning but also illustrate the crucial role of the Zr metal valence in the formation of collective electronic orders.

DOI: 10.1103/PhysRevB.106.165113

I. INTRODUCTION

Electronic correlations associated with charge density waves (CDWs) and superconductivity (SC), both the Fermi surface (FS) instabilities and low-temperature collective orders in solids, have attracted considerable attention [1–4]. In particular, layered van der Waals (vdW) transition metal chalcogenides have raised interest due to possible quantum critical phenomena [5,6]; yet due to relatively easy exfoliation, heteroepitaxial growth, and device fabrication of vdW crystals they can be used to investigate confinement of correlated electronic wave functions involved in CDWs and SC and also to engineer new quantum states [7–11].

$ZrTe_3$ provides a good platform due to its low-dimensional crystal structure with $P2_1/m$ unit cell symmetry [Fig. 1(a)]: Quasi-two-dimensional (quasi-2D) $ZrTe_3$ prisms aligned along the c axis are separated by the vdW gap with quasi-one-dimensional (quasi-1D) $ZrTe_6$ chains running along the b axis; in addition, there are Te2-Te3 chains along the a axis [12–14]. $ZrTe_3$ shows not only a CDW ($T_{\mathrm{CDW}} \sim 63$ K) with Peierls modulation $\mathbf{q} \approx (\frac{1}{14}, 0, \frac{1}{3})$ but also a filamentary SC ($T_{\mathrm{c}} \sim 2$ K) that arises on cooling from a quasi-2D electronic conduction (resistivity $\rho_a \approx \rho_b \sim \frac{\rho_c}{10}$) [15–18]. A local-pairs-induced SC mechanism was proposed [19]. Band structure calculations and angle-resolved photoemission spectroscopy (ARPES) measurements revealed that the FS consists mainly of a three-dimensional (3D) FS sheet centered at the Brillouin zone (BZ) center and quasi-1D FS sheets parallel to the inclination of the BZ boundary [20–24]. A pseudogap feature and CDW fluctuations persist far above T_{CDW} [25–27]. A Kohn anomaly associated with a soft phonon mode was identified [28], while the Raman experiment also emphasized the important role of electron-phonon (e-p) coupling at ambient or high pressure [29,30]. Additionally, a mixed valence of Zr in $ZrTe_3$ nanoribbons was reported [31]. Valence segregation with SC in transition metal oxides with different electron correlation strengths can be connected to the SC mechanism and the e-p coupling [32–35].

Bulk SC can be induced in $ZrTe_3$ by applying physical pressure, intercalation, doping, and disorder [36–47]. A pressure-induced reentrant SC in $ZrTe_3$ implies a possible unconventional SC mechanism [36], while the ultralow-temperature thermal conductivity indicates multiple nodeless

---

[*] Present address: Los Alamos National Laboratory, Los Alamos, New Mexico 87545, USA; yuliu@lanl.gov

[†] Present address: Anhui Province Key Laboratory of Condensed Matter Physics at Extreme Conditions, High Magnetic Field Laboratory, Chinese Academy of Sciences, Hefei 230031, China.

[‡] Present address: Department of Physics and Beijing Key Laboratory of Opto-electronic Functional Materials & Micro-nano Devices , Renmin University of China, Beijing 100872, China.

[§] Present address: ALBA Synchrotron Light Source, Cerdanyola del Vallès, E-08290 Barcelona, Spain.

[‖] petrovic@bnl.gov

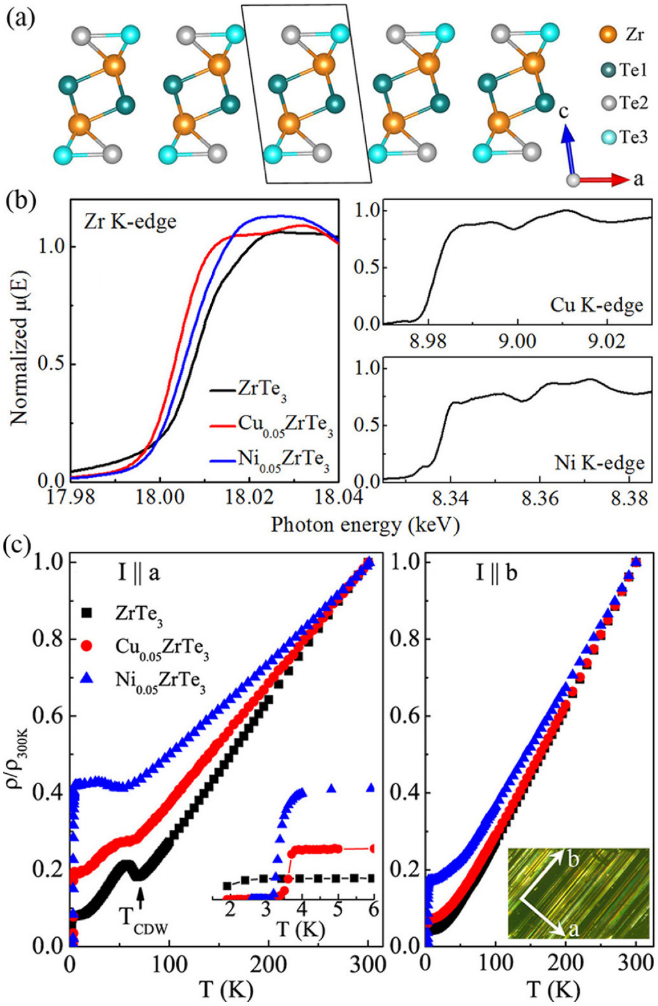

FIG. 1. (a) Crystal structure of $ZrTe_3$ with quasi-1D $ZrTe_6$ chains along the *b* axis and the Te2-Te3 rectangular network layer viewed from the *c* axis. (b) Normalized Zr (left) and Cu and Ni (right) *K*-edge XANES spectra at room temperature. (c) Temperature dependence of the normalized resistivity $\rho(T)/\rho(300\ \mathrm{K})$ for $ZrTe_3$ and $(Cu, Ni)_{0.05}ZrTe_3$ with the current flow along the *a* axis (left) and the *b* axis (right). Insets show the low-temperature superconducting transitions and current flow direction in crystals.

gaps in $ZrTe_{3-x}Se_x$ [44]. Light intercalation of ∼5% Cu and Ni can induce bulk SC with $T_c \sim 3.8$ and 3.1 K in $Cu_{0.05}ZrTe_3$ and $Ni_{0.05}ZrTe_3$, respectively, that coexists with the CDW order [39,40]. The CDW-related resistivity anomaly for the current flow along the *a* axis shifts to lower temperatures with reduced amplitudes; however, the optical absorption spectra show an increase in the CDW gap size in $(Cu, Ni)_{0.05}ZrTe_3$ [48].

Thermopower measurement is suitable to characterize the nature and sign of carriers as well as the correlation strength in superconductors, whereas x-ray photoemission spectroscopy (XPS) and Raman measurements are good probes of the valence state and phonon vibrations in transition metal compounds [49–53]. Herein we examine the electron correlation strength and the Zr valence in superconducting $(Cu, Ni)_{0.05}ZrTe_3$ single crystals. Thermal transport and Raman measurements show a suppressed CDW in $(Cu, Ni)_{0.05}ZrTe_3$ when compared with $ZrTe_3$. An obvious anomaly around T_{CDW} in thermal conductivity $\kappa(T)$ was observed in $ZrTe_3$, indicating strong e-p coupling. The anomaly is suppressed with weaker amplitudes in $(Cu, Ni)_{0.05}ZrTe_3$. A clear slope change in thermopower $S(T)$ corresponds to a FS reconstruction across the CDW transition. Both the ratio of T_c to the Fermi temperature T_F and the effective mass m^* rise in $(Cu, Ni)_{0.05}ZrTe_3$ when compared with $ZrTe_{2.96}Se_{0.04}$ imply an increase in electronic correlations of the bulk conducting states due to the contribution of Cu and Ni, in agreement with the first-principles calculations. Whereas intercalation in the vdW gap stabilizes bulk SC at the expense of CDW order, it coincides with drastic reduction of the Zr mixed valence and the expansion of the unit cell along the *a* and *c* directions as well as a rapid increase in the atomic concentration ratio of Zr^{2+} to Zr^{4+} induced by Cu and Ni intercalation. This affects the Zr 4*d*-derived electronic states near the Γ point in the Brillouin zone below the Fermi level.

II. EXPERIMENTAL DETAILS

High-quality single crystals of $ZrTe_3$ with ∼5% Cu and Ni intercalation were fabricated by the chemical vapor transport method [39,40]. X-ray absorption near-edge structure (XANES) measurements were performed at the 8-ID beamline of the National Synchrotron Light Source II at Brookhaven National Laboratory in the fluorescence mode. Thermal transport was measured in a Quantum Design PPMS-9 with the standard four-probe technique. Thermopower was measured by using a one-heater–two-thermometer setup with hooked copper leads using a silver paint contact directly on the crystals. The continuous measuring mode was adopted for thermopower measurement with the maximum heater power and period set as 50 mW and 1430 s, respectively, along with the maximum temperature rise of 3%. The relative error in our measurement for thermopower was below 5% based on a Ni standard measured under identical conditions. Sample dimensions were measured using an optical microscope, Nikon SMZ-800, with 10-μm resolution. Specific heat was measured in the warming procedure by the heat pulse relaxation method in PPMS-9.

XPS measurements were carried out in an ultrahigh-vacuum (UHV) system with 3×10^{-10} Torr base pressure, equipped with a SPECS Phoibos 100 spectrometer and a nonmonochromatized Al-K_α x-ray source ($h\nu = 1486.6$ eV). The XPS peak positions were calibrated using adventitious C 1*s* at 284.8 eV. Single-selected-point unpolarized Raman spectrum experiments were performed using a WITec alpha300 confocal Raman microscope equipped with a red laser ($\lambda = 633$ nm), an electron-multiplying CCD detector, and a 100× objective lens with numerical aperture (NA) of 0.9. The Raman-scattered light was focused onto a multimode fiber and monochromator with a 1800-line/mm grating. Samples for the room-temperature XPS were exfoliated in air and then were sputtered in UHV with 2×10^{-5} Torr of Ar^+ ions with kinetic energy of 2500 eV for 60 min in order to remove surface oxygen contamination. Samples for Raman experiments were freshly exfoliated.

First-principles calculations were performed using the Vienna *ab initio* simulation package (VASP) by relaxing the atomic positions simultaneously with changing the unit cell volume and shape [54]. The energy convergence criterion was 10^{-6} eV, while the interatomic forces were less than 0.02 eV/Å. The energy cutoff for plane waves was 480 eV, and the k-point network was $6 \times 9 \times 4$ with the Perdew-Burke-Ernzerhof functional revised for solids (PBEsol) as an exchange-correlation functional [55]. After lattice relaxation, the spin-orbit coupling (SOC) was included for both the density of states (DOS) and the band structure calculations. The band unfolding and the DOS figures were obtained using the VASPKIT program [56]. The high-symmetry points of the Brillouin zone were chosen in the same manner as in Ref. [45].

III. RESULTS AND DISCUSSION

The crystal structure of $\mathrm{ZrTe_3}$ [Fig. 1(a)] consists of $\mathrm{ZrTe_3}$ trigonal prism building blocks stacked along the b axis and forming an infinite quasi-1D chain [12,13]. The monoclinic unit cell contains two neighboring chains bound via the nearest interchain Zr-Te1 to form layers in the ab plane. On the other hand, Te2-Te3 atoms form a rectangular network with alternate distances of 2.79 and 3.10 Å along the a axis, and a single distance of 3.93 Å along the b axis. The 5% Cu and Ni intercalations induce expansion of the a- and c-axis lattice parameters, ∼0.2–0.3% for $\mathrm{Cu_{0.05}ZrTe_3}$ and ∼0.6–0.7% for $\mathrm{Ni_{0.05}ZrTe_3}$, respectively [39,40]. However, the b-axis lattice constant is nearly unchanged. Figure 1(b) shows the normalized Zr, Cu, and Ni K-edge XANES spectra measured at room temperature (RT). The Zr K-edge absorption energy at ∼18.008 keV for $\mathrm{ZrTe_3}$ indicates a dominant $\mathrm{Zr^{4+}}$ state [57]; it shifts to lower energies with Cu and Ni intercalation towards the $\mathrm{Zr^{2+}}$ state. A weak pre-edge feature was observed in the Cu and Ni spectra, which is absent in that of Zr; along with the similar shape of Cu and Ni XANES spectra, this confirms that Cu and Ni atoms are well hybridized and intercalated in the vdW gap rather than substituted at Zr sites [58].

A clear resistivity upturn was observed at $T_{\mathrm{CDW}} = 63$ K for $\mathrm{ZrTe_3}$, defined by the minimum point in $d\rho/dT$, with the current parallel to the a axis [Fig. 1(c)]. T_{CDW} is suppressed to 58 and 41 K for $\mathrm{Cu_{0.05}ZrTe_3}$ and $\mathrm{Ni_{0.05}ZrTe_3}$, respectively, with a reduced amplitude. The residual resistivity ratio (RRR) of ∼12.7 for $\mathrm{ZrTe_3}$ also decreases to 5.3 and 2.4 for $\mathrm{Cu_{0.05}ZrTe_3}$ and $\mathrm{Ni_{0.05}ZrTe_3}$, respectively, caused by increased disorder scattering. An abrupt resistivity drop is clearly seen, signaling the onset of SC, with zero resistivity at $T_c \approx 3.6$ and 3.1 K for $\mathrm{Cu_{0.05}ZrTe_3}$ and $\mathrm{Ni_{0.05}ZrTe_3}$, respectively. For the current parallel to the b axis, no CDW anomaly was observed, but SC remains for $\mathrm{(Cu, Ni)_{0.05}ZrTe_3}$, consistent with Refs. [39,40].

Figure 2(a) shows the temperature-dependent thermal conductivity $\kappa(T)$ with the heat pulse applied in the ab plane. The $\kappa(300\ \mathrm{K})$ shows a relatively low value of 1.63 $\mathrm{W\,K^{-1}\,m^{-1}}$ for $\mathrm{ZrTe_3}$, caused by the combination of low crystal symmetry and a chemical composition with heavy elements. A clear kink in $\kappa(T)$ is observed around T_{CDW} for $\mathrm{ZrTe_3}$, indicating strong e-p coupling. The value of $\kappa(300\ \mathrm{K})$ increases to ∼1.87 and ∼1.77 $\mathrm{W\,K^{-1}\,m^{-1}}$ for $\mathrm{Cu_{0.05}ZrTe_3}$ and $\mathrm{Ni_{0.05}ZrTe_3}$, respectively. In addition, $\kappa(T)$ is weakly temperature dependent at high temperatures; the absence of a commonly observed maximum in $\kappa(T)$ indicates a significant acoustic phonon scattering [59]. Figure 2(b) presents the temperature-dependent thermopower $S(T)$ for $\mathrm{ZrTe_3}$ and $\mathrm{(Cu, Ni)_{0.05}ZrTe_3}$ crystals. Above 100 K, there are weak changes in $S(T)$. With decreasing temperature, the $S(T)$ of $\mathrm{ZrTe_3}$ changes its slope at T_{CDW}, reflecting a FS reconstruction across the CDW transition. Then $S(T)$ changes its sign from negative to positive inside the CDW state featuring a peak value at ∼19(3) K, indicating a crossover behavior from dominant electronlike to dominant holelike conduction. Similar behavior is observed in $\mathrm{(Cu, Ni)_{0.05}ZrTe_3}$ but with reduced absolute values of S at high temperatures, showing an increase of the hole band contribution in $\mathrm{(Cu, Ni)_{0.05}ZrTe_3}$. It can be seen that T_{CDW} is suppressed to lower temperatures for $\mathrm{(Cu, Ni)_{0.05}ZrTe_3}$ when compared with $\mathrm{ZrTe_3}$, in line with the resistivity data [Fig. 1(c)]. It is plausible to consider both the electronic diffusion, S_{diff}, and phonon-drag, S_{drag}, contributions to thermopower in $\mathrm{ZrTe_3}$. The S_{drag} term usually gives $\propto T^3$ for $T \ll \Theta_{\mathrm{D}}$, $\propto 1/T$ for $T \gg \Theta_{\mathrm{D}}$, and a peak feature at $(\sim\frac{1}{4}\text{–}\frac{1}{5})\Theta_{\mathrm{D}}$. The peak feature in $\mathrm{ZrTe_3}$ cannot be simply attributed to only the phonon-drag effect since the peak temperature is lower than $\Theta_{\mathrm{D}}/5 \approx 36.6(1)$ K; this is also applicable for $\mathrm{(Cu, Ni)_{0.05}ZrTe_3}$ (see Table I). However, the phonon drag should diminish by $1/T$ at high temperatures, which is not seen here, pointing to the presence of a diffusion contribution as well. At low temperatures, the diffusive See-

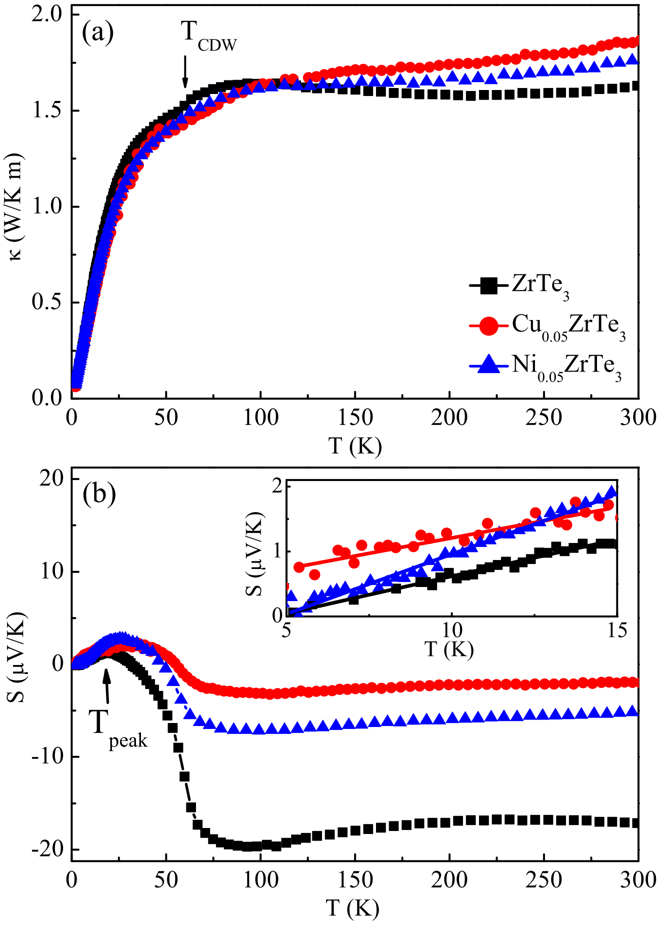

FIG. 2. Temperature-dependent (a) thermal conductivity $\kappa(T)$ and (b) thermopower $S(T)$ for the indicated samples. The inset in (b) shows the linear fit of $S(T)$ from 5 to 15 K.

TABLE I. A set of parameters derived from the thermopower $S(T)$ and specific heat $C_p(T)$ for the indicated single crystals.

Samples	S/T (μV/K^2)	γ (mJ mol^{-1} K^{-2})	q	T_c (K)	T_F (10^3 K)	T_c/T_F ($\times 10^{-3}$)	m^*/m_e	Θ_D (K)	T_{peak} (K)	T_{CDW} (K)
$ZrTe_3$	0.114(3)			2	3.7(1)	0.54(1)			19(3)	60(2)
$Cu_{0.05}ZrTe_3$	0.09(1)	2.6(1)	3.3(2)	3.6	4.7(5)	0.77(8)	2.2(1)	186(1)	30(5)	55(2)
$Ni_{0.05}ZrTe_3$	0.188(4)	2.7(1)	6.7(1)	3.1	2.3(1)	1.35(6)	2.8(1)	192.4(1)	26(3)	58(2)

beck response of the Fermi liquid dominates and is expected to be linear in T. In a single-band system, $S(T)$ is given by [60,61]

$$\frac{S}{T} = \pm\frac{\pi^2}{2}\frac{k_B}{e}\frac{1}{T_F} = \pm\frac{\pi^2}{3}\frac{k_B^2}{e}\frac{N(\varepsilon_F)}{n}, \tag{1}$$

where k_B is the Boltzmann constant, T_F is the Fermi temperature related to the Fermi energy ε_F and the density of states $N(\varepsilon_F)$ as $N(\varepsilon_F) = 3n/2\varepsilon_F = 3n/k_B T_F$, and n is the carrier concentration. In a multiband system it gives the upper limit of T_F of the dominant band. The derived S/T from 5 to 15 K [inset in Fig. 2(b)] is ~0.114(3) μV/K^2 for $ZrTe_3$ and ~0.09(1) and ~0.188(4) μV/K^2 for $Cu_{0.05}ZrTe_3$ and $Ni_{0.05}ZrTe_3$, respectively. Then we calculate $T_F \approx 3.7(1) \times 10^3$ K for $ZrTe_3$; $T_F \approx 4.7(5) \times 10^3$ and $2.3(1) \times 10^3$ K for $Cu_{0.05}ZrTe_3$ and $Ni_{0.05}ZrTe_3$, respectively. The ratio T_c/T_F characterizes the correlation strength in superconductors; T_c/T_F is ~0.1 in $Fe_{1+y}Te_{1-x}Se_x$, pointing to the importance of electron correlation, whereas it is ~0.02 in the BCS superconductor $LuNi_2B_2C$ [52]. Here, T_c/T_F is $\sim 0.54(1) \times 10^{-3}$ for $ZrTe_3$, and it is $\sim 0.77(8) \times 10^{-3}$ and $\sim 1.35(6) \times 10^{-3}$ for $Cu_{0.05}ZrTe_3$ and $Ni_{0.05}ZrTe_3$, respectively. This indicates not only a weak electron correlation strength but also a substantial enhancement in $(Cu, Ni)_{0.05}ZrTe_3$ when compared with $ZrTe_3$ (Table I).

The electronic specific heat can also be expressed as

$$\gamma = \frac{\pi^2}{2}k_B\frac{n}{T_F} = \frac{\pi^2}{3}k_B^2 N(\varepsilon_F). \tag{2}$$

Combining Eqs. (1) and (2) yields $S/T = \pm\gamma/ne$; the units are V/K for S, J K^{-2} m^{-3} for γ, and m^{-3} for n, respectively [51,62]. In order to compare different materials, it is common to express γ in J mol^{-1} K^{-2}. Then we can define a dimensionless quantity $q = \frac{S}{T}\frac{N_A e}{\gamma}$, where N_A is Avogadro's number; the calculated q are 3.3(2) and 6.7(1) for $Cu_{0.05}ZrTe_3$ and $Ni_{0.05}ZrTe_3$, respectively. Given the volume of unit cell of ~0.23 nm^3, we obtain the carrier density per volume $n \approx 1.3(1) \times 10^{21}$ cm^{-3} and $k_F \approx 3.4(1)$ nm^{-1} for $Cu_{0.05}ZrTe_3$; $n \approx 6.5(1) \times 10^{20}$ cm^{-3} and $k_F \approx 2.68(1)$ nm^{-1} for $Ni_{0.05}ZrTe_3$. The effective mass m^*, derived from $k_B T_F = \hbar^2 k_F^2/2m^*$, is 2.2(1) and 2.8(1) m_e for $Cu_{0.05}ZrTe_3$ and $Ni_{0.05}ZrTe_3$, respectively, where m_e is the electron mass. Both the ratio of T_c to the Fermi temperature T_F and the effective mass m^* rise in $(Cu, Ni)_{0.05}ZrTe_3$ when compared with $ZrTe_{2.96}Se_{0.04}$ [$T_c/T_F = 0.0016(1)$ and $m^* = 1.53(1)\, m_e$] [63], indicating the increase in the correlation strength with Cu and Ni intercalation when compared with Se substitution.

Figure 3(a) shows the Raman peaks for $ZrTe_3$ (~215 and ~155 cm^{-1}) [63,64], corresponding to A_g modes which involve atomic movements in the *ac* plane [29]. The mode at 155 cm^{-1} hosts momenta that have a larger component along the *a* axis of the Te2-Te3 chains. The conductive electrons belonging to the quasi-1D FS are mainly contributed by the Te $5p_x$ orbitals of the Te2-Te3 chains, which can only be scattered forward or backward along the Te2-Te3 chains. Consequently, phonons in this mode will experience stronger scattering with conduction electrons of the quasi-1D FS, causing the wide peak as observed due to strong e-p coupling by satisfying $\mathbf{q} \cdot \mathbf{v}_F \approx \omega_{qv}$, where $\mathbf{v}_F$ is the Fermi velocity and ω_{qv} is the phonon energy [29]. The mode at 215 cm^{-1} also involves the Te2-Te3 chains but does not exhibit a large linewidth like that at 155 cm^{-1}. This can be explained by the fact that this mode is not coupled with the quasi-1D conduction electrons and can only be affected by nonconductive 3D-like electrons [29]. The sharpness of this peak suggests the good crystallinity of $ZrTe_3$.

For $(Cu, Ni)_{0.05}ZrTe_3$, the mode at 215 cm^{-1} is almost unaffected; in contrast, the mode at 155 cm^{-1} is significantly modulated. The position of the highest peak redshift, ~12 cm^{-1} from 155 to 143 cm^{-1}, suggests tensile lattice deformation of the Te2-Te3 chains along the *a* or *c* axis. This is quantitatively consistent with the structure analysis that Cu and Ni intercalations induce expansion of the *a*- and *c*-axis lattice parameters. In addition, broad peaks at ~125 and ~170 cm^{-1} are resolved for $(Cu, Ni)_{0.05}ZrTe_3$. Weak Raman peaks at ~122 and ~177 cm^{-1} that also belong to the eight A_g modes in the *ac* plane were observed for pure $ZrTe_3$ at 70 K with a counter-rotating, circularly polarized laser [29]. Therefore the lattice modulation caused by Cu and Ni intercalations enabled these vibration modes to become

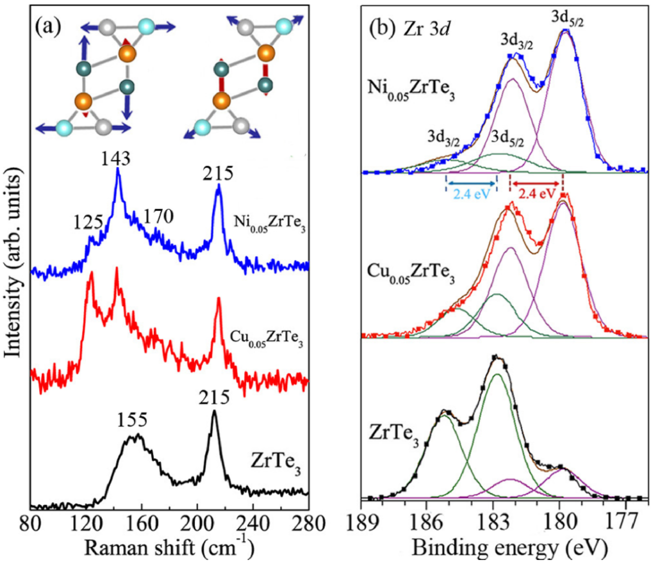

FIG. 3. (a) Raman peaks and (b) Zr 3*d* XPS spectra measured at room temperature for the indicated samples.

observable at RT here with an unpolarized laser. More importantly, the major peak at 143 cm^{-1} with narrow linewidth is much sharper compared with the corresponding peak for $\mathrm{ZrTe_3}$ at 155 cm^{-1}, which suggests the decoupling of quasi-1D conduction electrons with phonons at RT. This probably due to the e-p coupling condition of $\mathbf{q} \cdot \mathbf{v}_\mathrm{F} \approx \omega_{qv}$ being less satisfied since the phonon energy is reduced as a consequence of intercalation-induced lattice expansion. Thus the Raman results proved that the suppressed CDW is structural-distortion-driven suppression of the quasi-1D conductive e-p coupling. Structurally driven CDW suppression due to hydrostatic pressure and Se-doping-induced long-range disorder of lattices in the c and a axis, respectively, were also reported [30,63]. In these two cases, the suppression of e-p coupling was evidenced by the reduced Raman intensity ratio of the broad peak at 155 cm^{-1} to the peak at 215 cm^{-1}; structurally, the values of the lattice parameters in the c axis decreased or the size of the crystal unit cell was compressed. In $\mathrm{(Cu, Ni)_{0.05}ZrTe_3}$, in contrast, the suppression of e-p coupling is evidenced by the reduced linewidth of the major peak at 155 cm^{-1}; structurally, the lattice parameters in the a axis and c axis are expanded, indicating that CDW suppression can be realized through structural modulation in various pathways.

The XPS shows that both $\mathrm{ZrTe_3}$ and $\mathrm{(Cu, Ni)_{0.05}ZrTe_3}$ have mixed chemical states of $\mathrm{Zr^{4+}}$ and $\mathrm{Zr^{2+}}$ as evidenced by two sets of binding energies of Zr $3d_{5/2}$ and Zr $3d_{3/2}$ at ~183 and ~185.4 eV and at ~180 and ~182.4 eV [Fig. 3(b)]. However, the atomic concentration ratio of $\mathrm{Zr^{4+}}$ to $\mathrm{Zr^{2+}}$ is dramatically altered by the intercalation; the values of this ratio are 4.3, 0.32, and 0.23, for $\mathrm{ZrTe_3}$, $\mathrm{Cu_{0.05}ZrTe_3}$, and $\mathrm{Ni_{0.05}ZrTe_3}$, respectively. The average valence Zr is approximately +3.6 for $\mathrm{ZrTe_3}$, which decreases to approximately +2.5 for $\mathrm{Cu_{0.05}ZrTe_3}$ and +2.4 for $\mathrm{Ni_{0.05}ZrTe_3}$, respectively, in agreement with the trend in the XANES measurement. The Zr-Te bonds around Zr are spatially anisotropic in bond type and spatial distribution, causing a spatially anisotropic charge orbital environment around Zr and consequently an inhomogeneous Zr valence. The XANES and Raman results suggest that the lattice parameters of $\mathrm{ZrTe_3}$ are changed by Cu and Ni intercalations; thus the spatial anisotropic degree of Zr-Te bonds around Zr for $\mathrm{(Cu, Ni)_{0.05}ZrTe_3}$ can also be expected to be changed, resulting in the observed change in the ratio of $\mathrm{Zr^{4+}}$ to $\mathrm{Zr^{2+}}$. In contrast to the finding that unit cell reduction caused by Hf and Se doping is accompanied by a decreased $\mathrm{Zr^{2+}}$-to-$\mathrm{Zr^{4+}}$ ratio [30,63], unit cell expansion induced by Cu and Ni intercalations is accompanied by an increased $\mathrm{Zr^{2+}}$-to-$\mathrm{Zr^{4+}}$ ratio. Since 5% Ni induced a more expanded unit cell than Cu, the $\mathrm{Zr^{2+}}$-to-$\mathrm{Zr^{4+}}$ ratio also increased more. The hole-type 3D FS at the BZ center is mainly contributed by the Zr d orbital. ARPES shows that the 3D FS is slightly reduced in $\mathrm{ZrTe_{2.96}Se_{0.04}}$ when compared with $\mathrm{ZrTe_3}$ [65]. The reduced $\mathrm{Zr^{2+}}$-to-$\mathrm{Zr^{4+}}$ ratio in $\mathrm{ZrTe_{2.96}Se_{0.04}}$ [63] is coincident with the reduction of hole-type carrier numbers in the 3D band as confirmed by ARPES [65]; thus it is possible that $\mathrm{Zr^{2+}}$ contributed to the 3D FS though it is not much involved in the formation of the CDW. The quasi-1D FS responsible for the CDW and SC is mainly distributed on the BZ edge, in particular, in the D pocket [65], and is more sensitive to the change in BZ size modulated by lattice expansion or reduction.

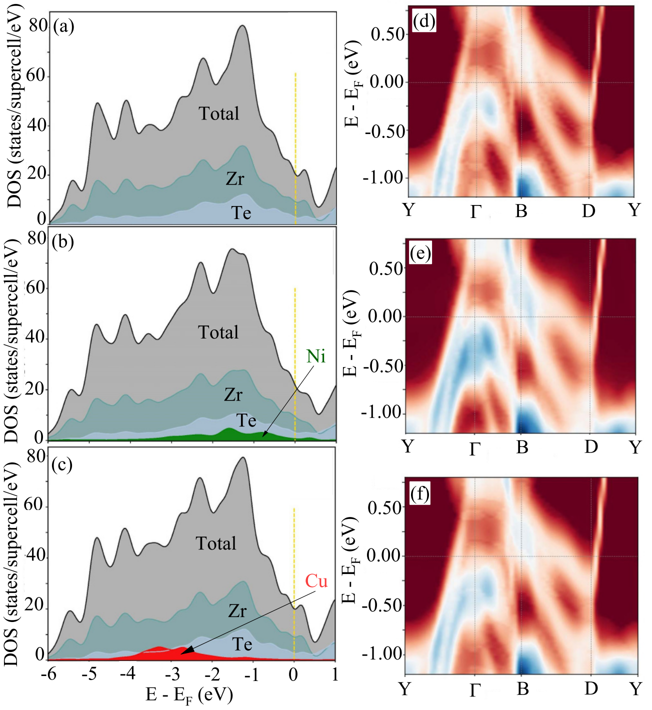

FIG. 4. Total and atomic contribution to density of states [(a)–(c)] and calculated band structures near Γ, B, D, and Y high-symmetry points [(d)–(f)] for $\mathrm{ZrTe_3}$, $\mathrm{Cu_{0.06}ZrTe_3}$, and $\mathrm{Ni_{0.06}ZrTe_3}$.

For insight into the impact of Cu and Ni intercalation we further performed comparative first-principles calculations of the density of states (DOS) [Figs. 4(a)–4(c)] and band structure [Figs. 4(d)–4(f)]. An intercalated atom in $\mathrm{ZrTe_3}$, either Cu or Ni, resides in a pentacoordinated Wyckoff $2e$ position within the vdW space gap. This position is in agreement with the most favorable interstitial position [45] as it is energetically favored when compared with tetrahedrally coordinated $2a$ and $2b$ positions. The calculated DOS for $\mathrm{ZrTe_3}$ [Fig. 4(a)] is in agreement with previous findings [66]. Upon intercalation, the Ni contribution to the DOS at the Fermi level is somewhat higher when compared with Cu [Figs. 4(b) and 4(c)], in agreement with the effective mass m^* (Table I). The effects of intercalation in the vdW gap of $\mathrm{ZrTe_3}$ are not substantial at the Fermi level. They are mainly visible in bands along the B-D high-symmetry direction as the increase in the spectral weight of the bands at energies (0.2–0.25) eV above the Fermi level, whereas quasi-1D band dispersion is unchanged between D and Y indicating negligible charge transfer from intercalated atoms to Te2-Te3 chains. On the other hand, we notice a shift near Γ for intercalated crystals [Figs. 4(e) and 4(f)] for the Zr $4d$-derived band at about −0.25 eV; the shift has been associated with Zr-Ni charge transfer in $\mathrm{Ni_xZrTe_3}$ [45].

For doped $\mathrm{ZrTe_3}$, the electronic structure of the quasi-1D FS, i.e., the FS nesting condition, is modulated via atomic structural modulation that is not spatially uniform throughout the entire $\mathrm{ZrTe_3}$ crystal. In other words, the lattice or BZ modulations are more likely in short-range order, consistent with the observation of reduced intensity or linewidth of the Raman peak at 155 to 143 cm^{-1} [Fig. 3(a)]. A long-range static CDW appears to compete with SC [67–69], while short-range CDW correlations are present over a substantial range of carrier concentrations [67,70] that support the appearance of SC. This can explain the higher T_c for Se-doped or Cu- and Ni-intercalated $ZrTe_3$ than that of pristine $ZrTe_3$. For Hf-doped $ZrTe_3$, because most of the Te2-Te3 chains are relaxed and thus the original lattice periodicity is kept, the long-range static CDW is preserved and is more stable at the cost of a reduced density of states of the quasi-1D band at the Fermi level; since a higher density of states is necessary for SC formation, this therefore renders suppressed SC. Compared with $TiSe_2$ [71] and other CDW materials, the SC can be substantially enhanced by Cu and Ni intercalation in $ZrTe_3$ while the CDW is only slightly suppressed. Recently, the thermal destruction of a CDW in $ZrTe_3$ studied by scanning tunneling microscopy (STM) has revealed a weak to strong impurity pinning across the CDW transition [72], calling for further STM studies on the effects of Hf,Se doping and Cu and Ni intercalation on the collective CDW and SC orders in $ZrTe_3$.

IV. CONCLUSIONS

In summary, 5% Cu and Ni intercalations in the vdW gap of $ZrTe_3$ result in an increase in T_c as well as the electron correlation strength. The ratio of Zr^{2+} atoms to Zr^{4+} atoms also increases, resulting in band shifts near the Γ point in the Brillouin zone. Intercalation results in a tensile lattice deformation of the Te2-Te3 atomic chains along the *a* or *c* axis and consequent expansion of the unit cell along these directions. This not only reduces the e-p coupling of the quasi-1D FS due to reduction of the phonon energy but also affects its nesting condition via atomic structural modulation, thus revealing the mechanism of CDW suppression. It exposes the important role of mixed valence in the competition of collective orders for the ground state at the Fermi surface.

ACKNOWLEDGMENTS

We thank Hengxin Tan and Binghai Yan for useful communications. Work at Brookhaven National Laboratory (BNL) is supported by the Office of Basic Energy Sciences, Materials Sciences and Engineering Division, U.S. Department of Energy, under Contract No. DE-SC0012704. This research used the 8-ID beamline of the National Synchrotron Light Source II and resources of the Center for Functional Nanomaterials, which is a U.S. Department of Energy Office of Science User Facility, at BNL under Contract No. DE-SC0012704. First-principles calculations were supported by the Ministry of Education, Science, and Technological Development of the Republic of Serbia.

[1] G. Grüner, The dynamics of charge-density waves, Rev. Mod. Phys. **60**, 1129 (1988).

[2] A. H. Castro Neto, Charge Density Wave, Superconductivity, and Anomalous Metallic Behavior in 2D Transition Metal Dichalcogenides, Phys. Rev. Lett. **86**, 4382 (2001).

[3] F. Schmitt, P. S. Kirchmann, U. Bovensiepen, R. G. Moore, L. Rettig, M. Krenz, J.-H. Chu, N. Ru, L. Perfetti, D. H. Lu, M. Wolf, I. R. Fisher, and Z.-X. Shen, Transient electronic structure and melting of a charge density wave in $TbTe_3$, Science **321**, 1649 (2008).

[4] S. A. Kivelson, E. Fradkin, and V. J. Emery, Electronic liquid-crystal phases of a doped Mott insulator, Nature (London) **393**, 550 (1998).

[5] H. Barath, M. Kim, J. F. Karpus, S. L. Cooper, P. Abbamonte, E. Fradkin, E. Morosan, and R. J. Cava, Quantum and Classical Mode Softening Near the Charge-Density-Wave-Superconductor Transition of Cu_xTiSe_2, Phys. Rev. Lett. **100**, 106402 (2008).

[6] Y. I. Joe, X. M. Chen, P. Ghaemi, K. D. Finkelstein, G. A. de la Pena, Y. Gan, J. C. T. Lee, S. Yuan, J. Geck, G. J. MacDougall, T. C. Chiang, S. L. Cooper, E. Fradkin, and P. Abbamonte, Emergence of charge density wave domain walls above the superconducting dome in 1T-$TiSe_2$, Nat. Phys. **10**, 421 (2014).

[7] A. K. Geremew, S. Rumyantsev, F. Kargar, B. Debnath, A. Nosek, M. A. Bloodgood, M. Bockrath, T. T. Salguero, R. K. Lake, and A. A. Balandin, Bias-voltage driven switching of the charge-density-wave and normal metallic phases in 1T-TaS_2 thin-film devices, ACS Nano **13**, 7231 (2019).

[8] Z. Zhang, J. Niu, P. Yang, Y. Gong, Q. Ji, J. Shi, Q. Fang, S. Jiang, H. Li, X. Zhou, L. Gu, X. Wu, and Y. Zhang, Van der Waals epitaxial growth of 2D metallic vanadium diselenide single crystals and their extra-high electrical conductivity, Adv. Mater. **29**, 1702359 (2017).

[9] C. B.- Constant, S. M.-Valero, R. Cordoba, and E. Coronado, Van der Waals heterostructures based on atomically-thin superconductors, Adv. Electron. Mater. **7**, 2000987 (2021).

[10] X. Zhou and E. E. Rodriguez, Tetrahedral transition metal chalcogenides as functional inorganic materials, Chem. Mater. **29**, 5737 (2017).

[11] G. H. Han, D. L. Duong, D. H. Keum, S. J. Yun, and Y. H. Lee, van der Waals metallic transition metal dichalcogenides, Chem. Rev. **118**, 6297 (2018).

[12] L. Brattås and A. Kjekshus, On the properties of compounds with the $ZrSe_3$ type structure, Acta Chem. Scand. **26**, 3441 (1972).

[13] S. Furuseth, L. Brattas, and A. Kjekshus, On the crystal structures of TiS_3, ZrS_3, $ZrSe_3$, $ZrTe_3$, HfS_3, and $HfSe_3$, Acta Chem. Scand. Ser. A **29**, 623 (1975).

[14] T. J. Wieting, A. Grisel, and F. Lévy, Lattice dynamical study of the low dimensional type B compounds TiS_3, $HfSe_3$, and $ZrTe_3$, Physica B+C (Amsterdam) **105**, 366 (1981).

[15] S. Takahashi, T. Sambongi, and S. Okada, Conduction properties of $ZrTe_3$, J. Phys., Colloq. **44**, 1733 (1983).

[16] D. J. Eaglesham, Electron microscope study of superlattices in $ZrTe_3$, J. Phys. C: Solid State Phys. **17**, L697 (1984).

[17] H. Nakajima, K. Nomura, and T. Sambongi, Anisotropic superconductiong transition in $ZrTe_3$, Physica B+C (Amsterdam) **143**, 240 (1986).

[18] K. Yamaya, Mixed bulk-filament nature in superconductivity of the charge-density-wave conductor $ZrTe_3$, Phys. Rev. B **85**, 184513 (2012).

[19] S. Tsuchiya, K. Matsubayashi, K. Yamaya, S. Takayanagi, S. Tanda, and Y. Uwatoko, Effects of pressure and magnetic field on superconductivity in $ZrTe_3$: Local pair-induced superconductivity, New J. Phys. **19**, 063004 (2017).

[20] K. Stöwe and F. R. Wagner, Crystal structure and calculated electronic band structure of $ZrTe_3$, J. Solid State Chem. **138**, 160 (1998).

[21] C. Felser, E. W. Finckh, H. Kleinke, F. Rocker, and W. Tremel, Electronic properties of $ZrTe_3$, J. Mater. Chem. **8**, 1787 (1998).

[22] P. Starowicz, C. Battaglia, F. Clerc, L. Despont, A. Prodan, H. J. P. van Midden, U. Szerer, A. Szytuta, M. G. Garnier, and P. I. Aebi, Electronic structure of $ZrTe_3$, J. Alloys Compd. **442**, 268 (2007).

[23] M. Hoesch, X. Cui, K. Shimada, C. Battaglia, S. Fujimori, and H. Berger, Splitting in the Fermi surface of $ZrTe_3$: A surface charge density wave system, Phys. Rev. B **80**, 075423 (2009).

[24] S. Lyu, L. Yu, J. Huang, C. Lin, Q. Gao, J. Liu, G. Liu, L. Zhao, J. Yuan, C. Chen, Z. Xu, and X. Zhou, Detailed electronic structure of three-dimensional Fermi surface and its sensitivity to charge density wave transition in $ZrTe_3$ revealed by high resolution laser-based angle-resolved photoemission spectroscopy, Chin. Phys. B **27**, 087503 (2018).

[25] A. Perucchi, L. Degiorgi, and H. Berger, Infrared signature of the charge-density wave gap in $ZrTe_3$, Eur. Phys. J. B **48**, 489 (2005).

[26] T. Yokoya, T. Kiss, A. Chainani, S. Shin, and K. Yamaya, Role of charge-density-wave fluctuations on the spectral function in a metallic charge-density-wave system, Phys. Rev. B **71**, 140504(R) (2005).

[27] M. Chinotti, J. Ethiraj, C. Mirri, X. Zhu, L. Li, C. Petrovic, and L. Degiorgi, Impact of the charge density wave state in the electrodynamic response of $ZrTe_{3-x}Se_x$: Optical evidence for a pseudogap phase, Phys. Rev. B **97**, 045117 (2018).

[28] M. Hoesch, A. Bosak, D. Chernyshov, H. Berger, and M. Krisch, Giant Kohn Anomaly and the Phase Transition in Charge Density Wave $ZrTe_3$, Phys. Rev. Lett. **102**, 086402 (2009).

[29] Y. Hu, F. Zheng, X. Ren, J. Feng, and Y. Li, Charge density waves and phonon-electron coupling in $ZrTe_3$, Phys. Rev. B **91**, 144502 (2015).

[30] S. L. Gleason, Y. Gim, T. Byrum, A. Kogar, P. Abbamonte, E. Fradkin, G. J. MacDougall, D. J. Van Harlingen, X. Zhu, C. Petrovic, and S. L. Cooper, Structural contributions to the pressure-tuned charge-density-wave to superconductor transition in $ZrTe_3$: Raman scattering studies, Phys. Rev. B **91**, 155124 (2015).

[31] X. Yu, X. Wen, W. Zhang, L. Yang, H. WU, X. Lou, Z. Xie, Y. Liu, and H. Chang, Fast and controlled growth of two-dimensional layered $ZrTe_3$ nanoribbons by chemical vapor deposition, CrystEngComm **21**, 5586 (2019).

[32] J. B. Goodenough, Perspective on engineering transition-metal oxides, Chem. Mater. **26**, 820 (2014).

[33] C. M. Varma, Mixed-valence compounds, Rev. Mod. Phys. **48**, 219 (1976).

[34] T. M. Rice and L. Sneddon, Real-Space and $\vec{k}$-Space Electron Pairing in $BaPb_{1-x}Bi_xO_3$, Phys. Rev. Lett. **47**, 689 (1981).

[35] M. Kim, S. Klenner, G. M. McNally, J. Nuss, A. Yaresko, U. Wedig, R. K. Kremer, R. Pöttgen, and H. Takagi, Mixed valence and superconductivity in perovskite antimonates, Chem. Mater. **33**, 6787 (2021).

[36] R. Yomo, Pressure effect on competition between charge density wave and superconductivity in $ZrTe_3$: Appearance of pressure induced reentrant superconductivity, Phys. Rev. B **71**, 132508 (2005).

[37] M. Hoesch, G. Garbarino, C. Battaglia, P. Aebi, and H. Berger, Evolution of the charge density wave superstructure in $ZrTe_3$ under pressure, Phys. Rev. B **93**, 125102 (2016).

[38] K. Gu, R. A. Susilo, F. Ke, W. Deng, Y. Wang, L. Zhang, H. Xiao, and B. Chen, Pressure-induced enhancement in the superconductivity of $ZrTe_3$, J. Phys.: Condens. Matter **30**, 385701 (2018).

[39] H. Lei, X. Zhu, and C. Petrovic, Raising T_c in charge density wave superconductor $ZrTe_3$ by Ni intercalation, Europhys. Lett. **95**, 17011 (2011).

[40] X. Zhu, H. Lei, and C. Petrovic, Coexistence of Bulk Superconductivity and Charge Density Wave in Cu_xZrTe_3, Phys. Rev. Lett. **106**, 246404 (2011).

[41] C. S. Yadav and P. L. Paulose, Superconductivity at 5.2 K in $ZrTe_3$ polycrystals and the effect of Cu and Ag intercalation, J. Phys.: Condens. Matter **24**, 235702 (2012).

[42] X. Zhu, B. Lv, F. Wei, Y. Xue, B. Lorenz, L. Deng, Y. Sun, and C. Chu, Disorder-induced bulk superconductivity in $ZrTe_3$ single crystals via growth control, Phys. Rev. B **87**, 024508 (2013).

[43] X. Zhu, W. Ning, L. Li, L. Ling, R. Zhang, J. Zhang, K. Wang, Y. Liu, L. Pi, Y. Ma, H. Du, M. Tian, Y. Sun, C. Petrovic, and Y. Zhang, Superconductivity and charge density wave in $ZrTe_{3-x}Se_x$, Sci. Rep. **6**, 26974 (2016).

[44] S. Cui, L. He, X. Hong, X. Zhu, C. Petrovic, and S. Li, Multiband nodeless superconductivity near the charge-density-wave quantum critical point in $ZrTe_{3-x}Se_x$, Chin. Phys. B **25**, 077403 (2016).

[45] A. M. Ganose, L. Gannon, F. Fabrizi, H. Nowell, S. A. Barnett, H. Lei, X. Zhu, C. Petrovic, D. O. Scanlon, and M. Hoesch, Local corrugation and persistent charge density wave in $ZrTe_3$ with Ni intercalation, Phys. Rev. B **97**, 155103 (2018).

[46] H. Yan, N. Shirato, X. Zhu, D. Rosenmann, X. Tong, W. Xu, C. Petrovic, V. Rose, and E. Nazaretski, X-ray assisted scanning tunneling microscopy and its application for materials science: the first results on Cu doped $ZrTe_3$, Crystals **9**, 588 (2019).

[47] L. Yue, S. Xue, J. Li, W. Hu, A. Barbour, F. Zheng, L. Wang, J. Feng, S. B. Wilkins, C. Mazzoli, R. Comin, and Y. Li, Distinction between pristine and disorder-perturbed charge density waves in $ZrTe_3$, Nat. Commun. **11**, 98 (2020).

[48] C. Mirri, A. Dusza, X. Zhu, H. Lei, H. Ryu, L. Degiorgi, and C. Petrovic, Excitation spectrum in Ni- and Cu-doped $ZrTe_3$, Phys. Rev. B **89**, 035144 (2014).

[49] C. Collignon, A. Ataei, A. Gourgout, S. Badoux, M. Lizaire, A. Legros, S. Licciardello, S. Wiedmann, J. Yan, J. Zhou, Q. Ma, B. D. Gaulin, N. Doiron-Leyraud, and L. Tillefer, Thermopower across the phase diagram of the cuprate $La_{1.6-x}Nd_{0.4}CuO_4$: Signatures of the pseudogap and charge density wave phases, Phys. Rev. B **103**, 155102 (2021).

[50] K. Wang, H. Lei, and C. Petrovic, Evolution of correlation strength in $K_xFe_{2-y}Se_2$ superconductor doped with S, Phys. Rev. B **84**, 054526 (2011).

[51] K. Behnia, D. Jaccard, and J. Flouquet, On the thermoelectricity of correlated electrons in the zero-temperature limit, J. Phys.: Condens. Matter. **16**, 5187 (2004).

[52] A. Pourret, L. Malone, A. B. Antunes, C. S. Yadav, P. L. Paulose, B. Fauque, and K. Behnia, Strong correlation and low carrier density in $Fe_{1+y}Te_{0.6}Se_{0.4}$ as seen from its thermoelectric response, Phys. Rev. B **83**, 020504(R) (2011).

[53] M. Demeter, M. Neumann, and W. Reichelt, Mixed-valence vanadium oxides studied by XPS, Surf. Sci. **454-456**, 41 (2000).

[54] G. Kresse and J. Furthmüller, Efficient iterative schemes for *ab initio* total-energy calculations using a plane-wave basis set, Phys. Rev. B **54**, 11169 (1996).

[55] J. P. Perdew, A. Ruzsinszky, C. Gábor, O. A. Vydrov, G. E. Scuseria, L. A. Constantin, X. Zhou, and K. Burke, Restoring the Density-Gradient Expansion for Exchange in Solids and Surfaces, Phys. Rev. Lett. **100**, 136406 (2008).

[56] V. Wang, N. Xu, J. Liu, G. Tang, and W. Geng, VASPKIT: A user-friendly interface facilitating high-throughput computing and analysis using VASP code, Comput. Phys. Commun. **267**, 108033 (2021).

[57] Z. Muhammad, B. Zhang, H. Lv, H. Shan, Z. Rehman, S. Chen, Z. Sun, X. Wu, A. Zhao, and L. Song, Transition from semimetal to semiconductor in $ZrTe_2$ induced by Se substitution, ACS Nano **14**, 835 (2020).

[58] T. E. Westre, P. Kennepohl, J. G. DeWitt, B. Hedman, K. O. Hodgson, and E. I. Solomon, A multiplet analysis of Fe K-edge $1s \rightarrow 3d$ pre-Edge features of iron complexes, J. Am. Chem. Soc. **119**, 6297 (1997).

[59] N. Barišić, I. Smiljanić, P. Popčević, A. Bilušić, E. Tutiš, A. Smontara, H. Berge, J. Jaćimović, O. Yuli, and L. Forró, High-pressure study of transport properties in $Co_{0.33}NbS_2$, Phys. Rev. B **84**, 075157 (2011).

[60] R. D. Barnard, *Thermoelectricity in Metals and Alloys* (Taylor & Francis, London, 1972).

[61] K. Miyake and H. Kohno, Theory of quasi-universal ratio of Seebeck coefficient to specific heat in zero-temperature limit in correlated metals, J. Phys. Soc. Jpn. **74**, 254 (2005).

[62] Y. Liu, Z. Hu, M. O. Ogunbunmi, E. Stavitski, K. Attenkofer, S. Bobev, and C. Petrovic, Giant thermoelectric power factor anisotropy in $PtSb_{1.4}Sn_{0.6}$, Inorg. Chem. **61**, 13586 (2022).

[63] Y. Liu, Z. Hu, X. Tong, D. Leshchev, X. Zhu, H. Lei, E. Stavitski, K. Attenkofer, and C. Petrovic, Thermal transport and mixed valence in $ZrTe_3$ doped with Hf and Se, Appl. Phys. Lett. **120**, 022601 (2022).

[64] S. Yang, H. Cai, B. Chen, C. Ko, V. O. Özçelik, D. F. Ogletree, C. E. White, Y. Shen, and S. Tongay, Environmental stability of 2D anisotropic tellurium containing nanomaterials: anisotropic to isotropic transition, Nanoscale **9**, 12288 (2017).

[65] M. Hoesch, L. Gannon, K. Shimada, B. J. Parrett, M. D. Watson, T. K. Kim, X. Zhu, and C. Petrovic, Disorder Quenching of the Charge Density Wave in $ZrTe_3$, Phys. Rev. Lett. **122**, 017601 (2019).

[66] Y. Kubo, Y. Sakurao, M. Ito, A. Koizumi, K. Yamaya, and Y. Uwatoko, Electron momentum density in the low-dimensional layered system $ZrTe_3$, J. Phys. Soc. Jpn. **76**, 064711 (2007).

[67] G. Ghiringhelli, M. Le Tacon, M. Minola, S. Blanco-Canosa, C. Mazzoli, N. B. Brookes, G. M. De Luca, A. Frano, D. G. Hawthorn, F. He, T. Loew, M. M. Sala, D. C. Peets, M. Salluzzo, E. Schierle, R. Sutarto, G. A. Sawatzky, E. Weschke, B. Keimer, and L. Braicovich, Long-range incommensurate charge fluctuations in $(Y,Nd)Ba_2Cu_3O_{6+x}$, Science **337**, 821 (2012).

[68] E. H. da Silva Neto, P. Aynajian, A. Frano, R. Comin, E. Schierle, E. Weschke, A. Gyenis, J. Wen, J. Schneeloch, Z. Xu, S. Ono, G. Gu, M. Le Tacon, and A. Yazdani, Ubiquitous interplay between charge ordering and high-temperature superconductivity in cuprates, Science **343**, 393 (2014).

[69] T. P. Croft, C. Lester, M. S. Senn, A. Bombardi, and S. M. Hayden, Charge density wave fluctuations in $La_{2-x}Sr_xCuO_4$ and their competition with superconductivity, Phys. Rev. B **89**, 224513 (2014).

[70] D. LeBoeuf, N. Doiron-Leyraud, B. Vignolle, M. Sutherland, B. J. Ramshaw, J. Levallois, R. Daou, F. Laliberté, O. Cyr-Choinière, J. Chang, Y. J. Yo, L. Balicas, R. Liang, D. A. Bonn, W. N. Hardy, C. Proust, and L. Taillefer, Lifshitz critical point in the cuprate superconductor $YBa_2Cu_3O_y$ from high-field Hall effect measurements, Phys. Rev. B **83**, 054506 (2011).

[71] F. Morosan, H. W. Zandbergen, B. S. Dennis, J. W. G. Bos, Y. Onose, T. Klimczuk, A. P. Ramirez, N. P. Ong, and R. J. Cava, Superconductivity in Cu_xTiSe_2, Nat. Phys. **2**, 544 (2006).

[72] L. Liu, C. Zhu, Z. Y. Liu, H. Deng, X. B. Zhou, Y. Li, Y. Sun, X. Huang, S. Li, X. Du, Z. Wang, T. Guan, H. Mao, Y. Su, R. Wu, J.-X. Yin, J.-G. Cheng, and S. H. Pan, Thermal Dynamic of Charge Density Wave Pinning in $ZrTe_3$, Phys. Rev. Lett. **126**, 256401 (2021).